

Neutron skin thickness for ^{nat}Pb , ^{159}Tb and effects of deformation on matter radii for Mg, Na, Ar isotopes

Shingo Tagami

Department of Physics, Kyushu University, Fukuoka 819-0395, Japan

Takaykui Myo

General Education, Faculty of Engineering, Osaka Institute of Technology, Osaka 535-8585, Japan

Masanobu Yahiro*

Department of Physics, Kyushu University, Fukuoka 819-0395, Japan

(Dated: June 25, 2025)

Background: Data on reaction cross section σ_R of proton scattering are available for ^{nat}Pb (natural lead) and ^{159}Tb . In addition, data on σ_R and/or interaction ones σ_I are available for Mg, Na, Ar isotopes.

Purpose: Our aim is to determine neutron skin thickness r_{skin} for ^{nat}Pb , ^{159}Tb and to investigate effects of deformation for Mg, Na, Ar isotopes.

Methods: We use the chiral (Kyushu) g -matrix folding model for lower energies and the folding model based on the Love-Franey (LF) t -matrix for higher energies.

Results: For ^{159}Tb , our skin value is $r_{\text{skin}} = 0.273 \pm 0.073$ fm. As for ^{24}Mg , our matter radius $r_m(\sigma_R) = 3.03 \pm 0.08$ fm determined from σ_R includes effects of deformation, whereas the corresponding $r_m(\sigma_I) = 2.79 \pm 0.15$ fm does not. Effects of deformation are seen for Mg isotopes, $^{21,23}\text{Na}$, ^{40}Ar .

Conclusion: Our result $r_{\text{skin}} = 0.271 \pm 0.008$ fm for ^{nat}Pb agrees with $r_{\text{skin}}^{208\text{Pb}}(\text{PREX-II}) = 0.283 \pm 0.071$ fm for ^{208}Pb , where we assume $A = 208$ for ^{nat}Pb .

I. INTRODUCTION

Horowitz *et al.* [1] proposed a direct measurement for neutron skin thickness $r_{\text{skin}} = r_n - r_p$, where r_n (r_p) is the root-mean-square radii of neutrons (protons).

The PREX collaboration reported [2]

$$r_{\text{skin}}^{208\text{Pb}}(\text{PREX-II}) = 0.283 \pm 0.071 \text{ fm.} \quad (1)$$

The CREX group also did [3]

$$\begin{aligned} r_{\text{skin}}^{48\text{Ca}}(\text{CREX}) \\ = 0.121 \pm 0.026 (\text{exp}) \pm 0.024 (\text{model}) \text{ fm.} \end{aligned} \quad (2)$$

The values of matter radii $r_m(\text{exp})$, neutron radii $r_n(\text{exp})$, $r_{\text{skin}}(\text{exp})$, $r_p(\text{exp})$ are tabulated in Table I for ^{208}Pb and ^{48}Ca .

TABLE I. Values of matter radii $r_m(\text{exp})$, neutron radii $r_n(\text{exp})$, $r_{\text{skin}}(\text{exp})$ together with $r_p(\text{exp})$ deduced from the electron scattering [4, 5]. The radii are shown in units of fm.

	$r_p(\text{exp})$	$r_m(\text{exp})$	$r_n(\text{exp})$	$r_{\text{skin}}(\text{exp})$
PREX-II	5.444	5.617 ± 0.044	5.727 ± 0.071	0.283 ± 0.071
CREX	3.385	3.456 ± 0.030	3.506 ± 0.050	0.121 ± 0.050

In Ref. [6], we extracted neutron skin thickness $r_{\text{skin}}^{208\text{Pb}} = 0.278 \pm 0.035$ fm and matter radius $r_m(\sigma_R) = 5.614 \pm$

0.022 fm from reaction cross sections σ_R on $p+^{208}\text{Pb}$ scattering, using the chiral (Kyushu) g -matrix folding model [7] with the proton and neutron densities calculated with Gogny-D1S HFB (D1S-GHFB) with angular momentum projection (AMP). Our skin value agrees with $r_{\text{skin}}^{208\text{Pb}}(\text{PREX-II})$. The D1S-GHFB+AMP as a beyond mean field theory is very difficult for odd nuclei. The difficulty is shown In Ref. [8].

For a nucleus having mass number A , neutron number N , proton number Z , the $r_{\text{skin}}(\text{exp})$ yields $r_n(\text{exp})$, $r_m(\text{exp})$, when $r_p(\text{exp})$ is obtainable from the electron scattering [4, 5]; note that $A r_m(\text{exp})^2 = N r_n(\text{exp})^2 + Z r_p(\text{exp})^2$. For the case of $r_{\text{skin}}(\text{exp}) = 0$, we obtain that $r_n(\text{exp}) = r_p(\text{exp}) = r_m(\text{exp})$. For the case of $r_{\text{skin}}(\text{exp}) \neq 0$, the ratio $[r_n(\text{exp}) - r_m(\text{exp})]/r_{\text{skin}}(\text{exp})$ are about 40 % for both the $r_{\text{skin}}^{208\text{Pb}}(\text{PREX-II})$ and the $r_{\text{skin}}^{48\text{Ca}}(\text{CREX})$. In general, $r_n(\text{exp}) - r_m(\text{exp})$ stems from $r_{\text{skin}}(\text{exp})$.

After this work, we extracted r_{skin} and matter radii r_m systematically.

We extracted the r_{skin} of $^{116,118,120,122,124}\text{Sn}$ from $p+^{116,118,120,122,124}\text{Sn}$ scattering [9]. As shown in Fig. 1, the central values of the experimental data of Ref. [9] slightly increase as A changes from $A = 116$ to $A = 124$. Note that the experimental data do not show a clear dependence on A from $A = 118$ to $A = 124$, since the uncertainties are relatively large (30%) and the D1S-GHFB+AMP points increase by 50% from $A = 118$ to $A = 124$.

* orion093g@gmail.com

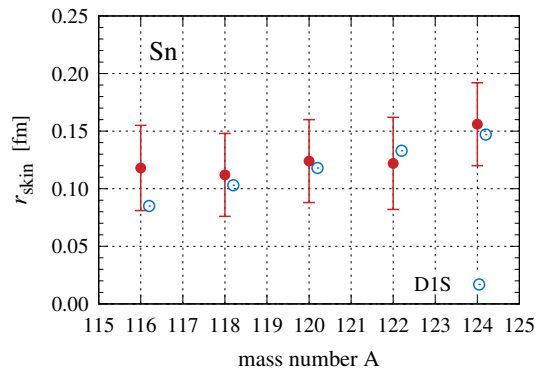


FIG. 1. Skin values of $^{116,118,120,122,124}\text{Sn}$ as a function of A . Closed circles with error-bar stand for our r_{skin} of p scattering for $^{116,118,120,122,124}\text{Sn}$ in Ref. [9]. Open circles denote the results calculated with D1S-GHFB+AMP.

The natural lead ^{nat}Pb is composed of ^{208}Pb (54.4%), ^{207}Pb (22.1%), ^{206}Pb (22.1%), ^{204}Pb (1.4%). Using our skin values for $^{116,118,120,122,124}\text{Sn}$, we predict that the skin values for $^{208,207,206,204}\text{Pb}$ are almost constant as a function of A . Prediction A indicates that the skin value for ^{nat}Pb is close to r_{skin}^{208} (PREX-II).

In this paper, we determine r_{skin} for ^{nat}Pb from the data on σ_{R} [10–16]. Whether the r_{skin} of ^{nat}Pb is close to $r_{\text{skin}}^{208\text{Pb}}$ (PREX-II) or not? In addition, we determine r_{skin} for ^{159}Tb from the data on σ_{R} [17] on $p+^{159}\text{Tb}$ scattering,

Suzuki *et al.* measured interaction cross sections σ_{I} for $^{20-23,25-32}\text{Na}+^{12}\text{C}$ and $^{20,22,23,27,29-32}\text{Mg}+^{12}\text{C}$ scattering at 950 MeV/u [18, 19] and determined matter radii $r_{\text{m}}(\sigma_{\text{I}})$ [19]. The measurement for Na isotopes was the first direct comparison between neutron radii r_{n} and proton ones r_{p} over a wide range of neutron number N , where the charge radii were determined by isotope-shift measurements [20]. As for $^{21,23}\text{Na}+^{12}\text{C}$ scattering, the reaction cross sections σ_{R} were measured by Zhang *et al.* at around 30 MeV/u [21].

There is an accumulation paper [22] for ^4He to ^{32}Mg . Data on σ_{I} at high energies, those on σ_{R} at low energies and the extracted $r_{\text{m}}(\sigma_{\text{I}})$ are accumulated; see Table 1 for the σ_{I} , Table 2 for the σ_{R} , Table 3 for the $r_{\text{m}}(\sigma_{\text{I}})$ that were by using Glauber model in the optical limit.

After the accumulation paper, Ozawa *et al.* measured σ_{I} for $^{32-40}\text{Ar}+^{12}\text{C}$ scattering at around 950 MeV/u, and extracted the proton skin thickness $r_{\text{skin,p}} = r_{\text{p}} - r_{\text{n}}$ and the $r_{\text{m}}(\sigma_{\text{I}})$ [23], using the Glauber-model calculations in the optical-limit approximation.

As an observable of determining r_{m} , r_{skin} , we can consider σ_{R} , σ_{I} . The $\sigma_{\text{R}}(\text{exp})$ is related to $\sigma_{\text{I}}(\text{exp})$ as

$$\sigma_{\text{I}}(\text{exp}) = \sigma_{\text{R}}(\text{exp}) - \sigma_{\text{inela}} \quad (3)$$

for the total inelastic cross sections σ_{inela} . The matter radius $r_{\text{m}}(\sigma_{\text{I}})$ extracted from σ_{I} is smaller than $r_{\text{m}}(\sigma_{\text{R}})$. There is possibility that $r_{\text{m}}(\sigma_{\text{I}})$ do not include effects of deformation, since large deformation induces strong excitation.

Takechi *et al.* made precise measurements on σ_{R} for $^{24-38}\text{Mg}$ on a ^{12}C target at energies around 240 MeV/u [24].

Watanabe *et al.* determined $r_{\text{m}}(\sigma_{\text{R}})$ for $^{24-38}\text{Mg}$ [25]. The ground-state properties of Mg isotopes based on D1S-AMD (antisymmetrized molecular dynamics) are shown in Ref. [25]. For Mg isotopes, the $r_{\text{m}}(\sigma_{\text{R}})$ of Ref. [25] and the $r_{\text{m}}(\sigma_{\text{I}})$ of Ref. [22] were tabulated; Table II shows these values for ^{24}Mg . There is non-negligible difference between them. This point is investigated in this paper for Mg isotopes.

TABLE II. Comparison between our values $r_{\text{m}}(\sigma_{\text{R}})$ of Refs. [25–27] and $r_{\text{m}}(\sigma_{\text{I}})$ of Ref. [22]. The radii are shown in units of fm.

	$r_{\text{m}}(\sigma_{\text{I}})$	$r_{\text{m}}(\sigma_{\text{R}})$
^6He	2.48 ± 0.03	2.48 ± 0.03
^8He	2.52 ± 0.03	2.53 ± 0.02
^{12}C	2.35 ± 0.02	2.352 ± 0.013
^{24}Mg	2.79 ± 0.15	3.03 ± 0.08
^{27}Al		2.936 ± 0.012

Takechi *et al.* made precise measurements on σ_{R} for ^{12}C on ^9Be , ^{12}C , ^{27}Al targets in the wide incident-energy range of $E_{\text{lab}} = 30\text{--}400$ MeV/u [28]. Using the precise data for $^{12}\text{C}+^{12}\text{C}$ scattering, we tested the Kyushu g -matrix folding model for $^{12}\text{C}+^{12}\text{C}$ scattering, and found that the model is reliable for σ_{R} in $30 \leq E_{\text{lab}} \leq 100$ MeV/u and $250 \leq E_{\text{lab}} \leq 400$ MeV/u [8]. Note that no data is available in $E_{\text{lab}} \leq 30$ MeV/u.

The chiral nucleon-nucleon interactions used in the Kyushu g -matrix folding model have a cutoff of $\Lambda = 550$ MeV; the cutoff effects appear $450 \leq E_{\text{lab}} \leq 550$ MeV for the σ_{R} of $^{12}\text{C}+^{12}\text{C}$ scattering.

We tested the Kyushu g -matrix folding model [7] for proton scattering and found that the chiral (Kyushu) g -matrix folding model is reliable for $\sigma_{\text{R}}(\text{exp})$ in $20 \leq E_{\text{lab}} \leq 180$ MeV [29]. For this reason, the model is applicable for $E_{\text{lab}} \leq 450$ MeV. In $E_{\text{lab}} \geq 550$ MeV/u, we use the folding model based on Love-Franey (LF) t -matrix [30].

Takechi *et al.* also measured σ_{I} for $^{20-32}\text{Ne}+^{12}\text{C}$ scattering at around 240 MeV/u [31]. Minomo *et al.* used the D1S-AMD+RGM method to describe the tail of the last neutron of ^{31}Ne , where RGM stands for the resonating group method and AMD is antisymmetrized molecular dynamics. The theoretical prediction reproduces the measured σ_{I} of $^{28-32}\text{Ne}$ with no adjustable parameter [32]. The theoretical result indicates that the ground state of ^{31}Ne is a “deformed” halo nucleus with $(3/2)^-$. The ground-state properties of Ne isotopes based on AMD are shown in Ref [33].

From the precise data on the σ_{R} of Ref. [28], we extracted $r_{\text{m}}(\sigma_{\text{R}})$ for ^{12}C and ^{27}Al [26], using the chiral (Kyushu) g -matrix folding model [7]. In Ref. [27], we also determined $r_{\text{m}}(\sigma_{\text{R}})$ for $^{6,8}\text{He}$ from σ_{R} of $p+^{6,8}\text{He}$ scattering at 700 MeV, using the folding model based on Love-Franey (LF) t -matrix [30]. As shown in Table II, our values for $^{6,8}\text{He}$ are consistent with the corresponding values $r_{\text{m}}(\sigma_{\text{I}})$ shown in the accumulation paper. This consistency indicates that the Kyushu g -matrix folding model and the LF folding model are reliable.

In Ref. [29], we extracted r_{skin} and $r_m(\sigma_R)$ from σ_R of p scattering on ^{208}Pb , ^{58}Ni , $^{48,40}\text{Ca}$, ^{12}C targets, using the Kyushu g -matrix folding model. As a way of determining a fine-tuning factor f , we proposed the ESP-f (experimental scaling procedure). The ESP-f is a reliable way of r_{skin} and $r_m(\sigma_R)$. Our skin values of ^{208}Pb and ^{48}Ca are consistent with the PREX-II value [2] and the CREX one [3], respectively.

Tanaka *et al.* measured σ_I for $^{42-51}\text{Ca}+^{12}\text{C}$ scattering at 280 MeV/u, and determined matter radii $r_m(\sigma_I)$, neutron radii $r_n(\sigma_I)$, neutron skin thickness r_{skin} for $^{42-51}\text{Ca}$ from the σ_I , using the optical limit of the Glauber model with the Woods-Saxon densities [34]. We reanalyze the scattering to determine $r_m(\sigma_I)$, $r_n(\sigma_I)$, r_{skin} for $^{42-51}\text{Ca}$ in Ref. [35], using the Kyushu g -matrix folding model with the proton and neutron densities calculated with D1S-GHFB with and without AMP. Our values are consistent with theirs.

In this paper, our aim is to determine neutron skin thickness r_{skin} for ^{nat}Pb , ^{159}Tb and to investigate effects of deformation for Mg, Na, Ar isotopes. Our analyses are summarized blow.

- 1) **$p+^{nat}\text{Pb}$ scattering:** We extract r_{skin} and $r_m(\sigma_R)$ from data σ_R [10–16] in $E_{\text{lab}} = 21.1 \sim 341$ MeV, using the Kyushu g -matrix folding model with the D1S-GHFB+AMP proton and neutron densities. We assume $A = 208$ for ^{nat}Pb .
- 2) **$p+^{159}\text{Tb}$ scattering:** We extract r_{skin} and $r_m(\sigma_R)$ from data σ_R [17] in $20 \leq E_{\text{lab}} \leq 47.5$ MeV, using the Kyushu g -matrix folding model with the D1S-GHFB densities.
- 3-1) **$^{20-32}\text{Na}+^{12}\text{C}$ scattering:** We determine $r_m(\sigma_I)$ for $^{20-32}\text{Na}$ on the data σ_I [18, 19] at 950 MeV/u, using the LF t -matrix folding model with the Sly7 densities, where SLy7 [36–38] is an improved version of SLy4.
- 3-2) **$^{21,23}\text{Na}+^{12}\text{C}$ scattering:** We determine $r_m(\sigma_R)$ for $^{21,23}\text{Na}$ on data σ_R [21] at around 30 MeV/u, using the Kyushu g -matrix folding model with the Sly7 densities.
- 4) **Comparison between $r_m(\sigma_R)$ and $r_m(\sigma_I)$ for Mg isotopes:** We analyzed $^{24-38}\text{Mg}+^{12}\text{C}$ scattering at 240 MeV/u and determined the $r_m(\sigma_R)$ for $^{24-38}\text{Mg}$ [25]. Meanwhile, Suzuki *et al.* measured σ_I for $^{20,22,23,27,29-32}\text{Mg}+^{12}\text{C}$ scattering at 950 MeV/u [18, 19] and determined matter radii $r_m(\sigma_I)$ [19]. We find that the $r_m(\sigma_I)$ of Ref. [19] yield do not include effects of deformation, but the $r_m(\sigma_R)$ of Ref. [25] include effects of deformation; see Fig. 5. This is investigated with D1S-GHFB+AMP and the D1S-GHFB+AMP in the spherical limit.
- 5-1) **$^{32-40}\text{Ar}+^{12}\text{C}$ scattering:** We determine $r_m(\sigma_I)$ and $r_{\text{skin},p}$ for $^{32-40}\text{Ar}$ from the σ_I at around 950 MeV/u [23], using the LF folding model with the Sly7 densities.
- 5-2) **$p+^{40}\text{Ar}$ scattering:** We extract r_{skin} and $r_m(\sigma_R)$ from data σ_R [39] in $22.9 \leq E_{\text{lab}} \leq 46.9$ MeV, using the Kyushu g -matrix folding model with the Sly7 densities.

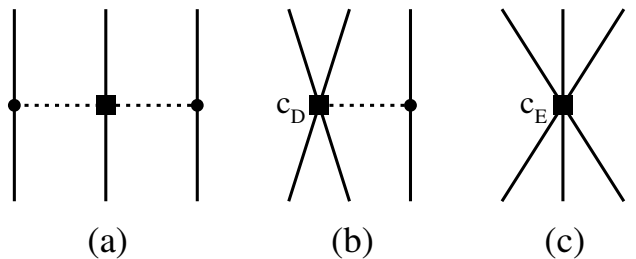


FIG. 2. 3NFs in NNLO. Diagram (a) corresponds to the Fujita-Miyazawa 2π -exchange 3NF [50], and diagrams (b) and (c) correspond to 1π -exchange and contact 3NFs. The solid and dashed lines denote nucleon and pion propagations, respectively, and filled circles and squares stand for vertices. The strength of the filled-square vertex is often called c_D in diagram (b) and c_E in diagram (c).

Our model is formulated in Sec. II, and our results are shown in Sec. III. Section IV is devoted to a summary.

II. MODEL

A. The g -matrix folding model

The g -matrix folding model [7, 25, 40–47] is a standard way of determining r_{skin} and r_m from σ_R and σ_I . The formulation of the g -matrix folding model is established, as shown in Refs. [7, 25, 40–43, 45–47]. In the model, the potential is obtained by folding the g -matrix with projectile (P) densities and target (T) ones.

The g -matrix folding model consists of the single-folding model (SFM) for nucleon-nucleus scattering and the double-folding model (DFM) for nucleus-nucleus scattering. Satchler succeeded in reproducing most of elastic nucleus-nucleus scattering with the the central direct and the central particle-exchange folding potential [48]. After the work, the SFM has the central and the spin-orbit folding potential, whereas the DFM has the central potential only.

Applying the folding model based on the Melbourne g -matrix [41] for σ_R of Mg isotopes, we deduced the $r_m(\sigma_R)$ for Mg isotopes [25], and discovered that ^{31}Ne is a halo nucleus with large deformation [32].

Kohno calculated the g matrix for the symmetric nuclear matter, using the Brueckner-Hartree-Fock method with chiral N^3LO 2NFs and NNLO 3NFs [49]. The chiral interactions mentioned above are explained in Fig. 2. He set $c_D = -2.5$ and $c_E = 0.25$ so that the energy per nucleon can become minimum at $\rho = \rho_0$ [7].

Toyokawa *et al.* localized the non-local chiral g matrix into three-range Gaussian forms by using the localization method proposed by the Melbourne group [41, 51, 52]. The resulting local g matrix is called “Kyushu g -matrix”.

The Kyushu g -matrix folding model is successful in reproducing $d\sigma/d\Omega$ and A_y for polarized proton scattering on var-

ious targets at $E_{\text{lab}} = 65$ MeV [46] and $d\sigma/d\Omega$ for ^4He scattering at $E_{\text{lab}} = 72$ MeV/u [47]. This is true for σ_{R} of ^4He scattering in $E_{\text{lab}} = 30 \sim 200$ MeV/u [7].

We use the Kyushu g -matrix folding model [7] and the LF folding model for nucleus-nucleus (PT) scattering, nucleon-nucleus (NT) scattering

B. Single-folding model

We consider proton as a projectile. Proton elastic scattering can be described by the one-body Schrödinger equation,

$$(T_{\text{R}} + U(\mathbf{R}) - E)\Psi^{(+)} = 0, \quad (4)$$

with a folded potential $U(\mathbf{R})$, where E is an energy of incident proton in the center of mass system and T_{R} is a kinetic-energy operator concerning the relative coordinate \mathbf{R} between an incident proton and a target. The optical potential U can be divided into the central (CE), the spin-orbit (LS), and the Coulomb (Coul) component as follows:

$$U(\mathbf{R}) = U_{\text{CE}} + U_{\text{LS}}\mathbf{L} \cdot \boldsymbol{\sigma} + V_{\text{Coul}}. \quad (5)$$

In the g -matrix folding model, U consists of the direct and particle-exchange parts. The exchange part is nonlocal, but it can be localized with the Brieva-Rook approximation [40]. Validity of the approximation is shown in Ref. [53].

The central part U_{CE} is then described by the sum of the direct component $U_{\text{CE}}^{\text{DR}}$ and the localized exchange component $U_{\text{CE}}^{\text{EX}}$ [40, 42, 54],

$$U_{\text{CE}} \equiv V_{\text{CE}} + iW_{\text{CE}} = U_{\text{CE}}^{\text{DR}} + U_{\text{CE}}^{\text{EX}} \quad (6)$$

with

$$U_{\text{CE}}^{\text{DR}}(\mathbf{R}) = \sum_{\alpha=p,n} \int \rho_{\alpha}(\mathbf{r}) g_{p\alpha}^{\text{DR}}(s; \rho_{\alpha}) d\mathbf{r}, \quad (7)$$

$$U_{\text{CE}}^{\text{EX}}(\mathbf{R}) = - \sum_{\alpha=p,n} \int \rho_{\alpha}(\mathbf{r}, \mathbf{r} - \mathbf{s}) g_{p\alpha}^{\text{EX}}(s; \rho_{\alpha}) j_0(K(R)s) d\mathbf{r}, \quad (8)$$

where V_{CE} (W_{CE}) is the real (imaginary) part of U_{CE} and $\mathbf{s} = \mathbf{r} - \mathbf{R}$, and \mathbf{r} is the coordinate of an interacting nucleon from the center-of-mass (c.m.) of target. The local momentum $\hbar K(R) \equiv \sqrt{2\mu_{\text{R}}(E - U_{\text{CE}} - V_{\text{Coul}})}$ present in Eq. (8) is obtained self-consistently, where μ_{R} is the reduced mass of the proton+target system.

The direct and exchange parts, $g_{p\alpha}^{\text{DR}}$ and $g_{p\alpha}^{\text{EX}}$, depend on the local density

$$\rho_{\alpha} = \rho_{\text{P}}^{\nu}(\mathbf{r}_{\text{T}} + \mathbf{s}/2) \quad (9)$$

at the midpoint of the interacting nucleon pair.

The direct part $g_{p\alpha}^{\text{DR}}$ and the exchange part $g_{p\alpha}^{\text{EX}}$ of the g -matrix interaction are assumed to be a function of the local density $\rho_{\alpha} = \rho_{\alpha}(\mathbf{r} - \mathbf{s}/2)$ at the midpoint of the interacting nucleon pair. The direct and exchange parts are described as

$$g_{pp}^{\text{DR,EX}}(s; \rho_p) = \frac{1}{4} (\pm g^{01} + 3g^{11}), \quad (10)$$

$$g_{pn}^{\text{DR,EX}}(s; \rho_n) = \frac{1}{8} (g^{00} \pm g^{01} \pm 3g^{10} + 3g^{11}), \quad (11)$$

in terms of the spin-isospin component g^{ST} of the g -matrix interaction.

Similar derivation is possible for the spin-orbit part U_{LS} [42],

$$U_{\text{LS}} \equiv V_{\text{LS}} + iW_{\text{LS}} = U_{\text{LS}}^{\text{DR}} + U_{\text{LS}}^{\text{EX}} \quad (12)$$

with

$$U_{\text{LS}}^{\text{DR}}(\mathbf{R}) = -\frac{1}{4R^2} \sum_{\alpha=p,n} \int \mathbf{R} \cdot \mathbf{s} \rho_{\alpha}(\mathbf{r}) g_{\text{LS},p\alpha}^{\text{DR}}(s; \rho_{\alpha}) d\mathbf{r}, \quad (13)$$

$$U_{\text{LS}}^{\text{EX}}(\mathbf{R}) = -\pi \sum_{\alpha=p,n} \int ds s^3 \left[\frac{2j_0(K(R)s)}{R} \rho_1^{(\alpha)}(R, s) + \frac{j_1(K(R)s)}{2k} \delta_0^{(\alpha)}(R, s) \right], \quad (14)$$

where V_{LS} (W_{LS}) is the real (imaginary) part of U_{LS} ; see Appendix A for the definition of $\rho_1^{(\alpha)}(R, s)$ and $\delta_0^{(\alpha)}(R, s)$. As a g -matrix, we take the Kyushu g -matrix resented in Ref. [7].

The matter radius r_{m} is defined with the ground-state wave function $\Phi_{\text{g.s.}}$ of T as

$$\begin{aligned} r_{\text{m}}^2 &\equiv \langle \Phi_{\text{g.s.}} | \sum_i \mathbf{r}_i^2 | \Phi_{\text{g.s.}} \rangle, \\ &= \int d\mathbf{r}_{\text{m}'} \langle \Phi_{\text{g.s.}} | \sum_i \mathbf{r}_i^2 \delta(\mathbf{r}_i - \mathbf{r}_{\text{m}'}) | \Phi_{\text{g.s.}} \rangle \\ &= \int d\mathbf{r}_{\text{m}'} \mathbf{r}_{\text{m}'}^2 \rho(\mathbf{r}_{\text{m}'}) \end{aligned} \quad (15)$$

for the one-body matter density

$$\rho(\mathbf{r}_{\text{m}}) = \langle \Phi_{\text{g.s.}} | \sum_i^A \delta(\mathbf{r}_i - \mathbf{r}_{\text{m}}) | \Phi_{\text{g.s.}} \rangle \quad (16)$$

Proton one-body density is

$$\rho(\mathbf{r}_{\text{p}}) = \langle \Phi_{\text{g.s.}} | \sum_j^Z \delta(\mathbf{r}_j - \mathbf{r}_{\text{p}}) | \Phi_{\text{g.s.}} \rangle, \quad (17)$$

where j is the j -th proton. Neutron one-body density is

$$\rho(\mathbf{r}_{\text{n}}) = \langle \Phi_{\text{g.s.}} | \sum_{j'}^N \delta(\mathbf{r}_{j'} - \mathbf{r}_{\text{n}}) | \Phi_{\text{g.s.}} \rangle, \quad (18)$$

where j' is the j' -th neutron.

The S -matrices are obtained by solving Eq. (4). This point is explained simply by switching off the spin-orbit potential, since the spin-orbit potential little affects σ_{R} . The σ_{R} are determined from the S -matrices as

$$\sigma_{\text{R}} = \frac{\pi}{k^2} \sum_L (2L+1)(1 - |S_L|^2), \quad (19)$$

where k is a wave number and L is an angular momentum with respect to \mathbf{R} .

The U_{CE} depends on $\rho(\mathbf{r}_{\text{p}})$ and $\rho(\mathbf{r}_{\text{n}})$, as shown in Eq. (7) an Eq. (8). The S -matrices depends on the U_{CE} . The σ_{R} depends on the S -matrices.

There is an empirical relation $\sigma_{\text{R}} = c r_{\text{m}}^2$ between r_{m} and σ_{R} . Note that a constant c is obtained from the calculated σ_{R} and r_{m} .

C. Double-folding model

Nucleus-nucleus (PT) elastic scattering can be described by the one-body Schrödinger equation,

$$(T_R + U_{CE}(\mathbf{R}) + V_{Coul} - E)\Psi^{(+)} = 0 \quad (20)$$

with the central; folded potential $U_{CE}(\mathbf{R})$ shown blow. Solving Eq. (20), we can get the S -matrices.

The folded potential $U_{CE}(\mathbf{R})$ is composed of the direct and exchange part, $U^{DR} + U^{EX}$, defined by

$$U^{DR}(\mathbf{R}) = \sum_{\mu,\nu} \int \rho_P^\mu(\mathbf{r}_P) \rho_T^\nu(\mathbf{r}_T) g_{\mu\nu}^{DR}(s; \rho_{\mu\nu}) d\mathbf{r}_P d\mathbf{r}_T, \quad (21)$$

$$U^{EX}(\mathbf{R}) = \sum_{\mu,\nu} \int \rho_P^\mu(\mathbf{r}_P, \mathbf{r}_P - \mathbf{s}) \rho_T^\nu(\mathbf{r}_T, \mathbf{r}_T + \mathbf{s}) \times g_{\mu\nu}^{EX}(s; \rho_{\mu\nu}) \exp[-i\mathbf{K}(\mathbf{R}) \cdot \mathbf{s}/M_A] d\mathbf{r}_P d\mathbf{r}_T \quad (22)$$

where $\mathbf{s} = \mathbf{r}_P - \mathbf{r}_T + \mathbf{R}$ for the coordinate \mathbf{R} between P and T and $M_A = AA_T/(A + A_T)$ for the mass number A (A_T) of P (T). The coordinate \mathbf{r}_P (\mathbf{r}_T) stands for the location of an interacting nucleon from the center-of-mass of the projectile (target). The projectile (target) densities $\rho_P^\mu(\mathbf{r}_P)$ ($\rho_T^\mu(\mathbf{r}_T)$) has the z component μ (ν) of the isospin. The local momentum $\hbar K(R) \equiv \sqrt{2\mu_R(E - U_{CE} - V_{Coul})}$ present in Eq. (22) is obtained self-consistently, where μ_R is the reduced mass of the PT system.

The direct and exchange parts, $g_{\mu\nu}^{DR}$ and $g_{\mu\nu}^{EX}$, depend on the local density

$$\rho_{\mu\nu} = \sigma^\mu [\rho_T^\nu(\mathbf{r}_T + \mathbf{s}/2) + \rho_P^\nu(\mathbf{r}_P - \mathbf{s}/2)] \quad (23)$$

at the midpoint of the interacting nucleon pair, where σ^μ is the Pauli matrix of a nucleon in P.

The direct and exchange parts are described by

$$g_{\mu\nu}^{DR}(s; \rho_{\mu\nu}) = \begin{cases} \frac{1}{4} \sum_S \hat{S}^2 g_{\mu\nu}^{S1}(s; \rho_{\mu\nu}) & ; \text{ for } \mu + \nu = \pm 1 \\ \frac{1}{8} \sum_{S,T} \hat{S}^2 g_{\mu\nu}^{ST}(s; \rho_{\mu\nu}), & ; \text{ for } \mu + \nu = 0 \end{cases} \quad (24)$$

$$g_{\mu\nu}^{EX}(s; \rho_{\mu\nu}) = \begin{cases} \frac{1}{4} \sum_S (-1)^{S+1} \hat{S}^2 g_{\mu\nu}^{S1}(s; \rho_{\mu\nu}) & ; \text{ for } \mu + \nu = \pm 1 \\ \frac{1}{8} \sum_{S,T} (-1)^{S+T} \hat{S}^2 g_{\mu\nu}^{ST}(s; \rho_{\mu\nu}) & ; \text{ for } \mu + \nu = 0 \end{cases} \quad (25)$$

where $\hat{S} = \sqrt{2S+1}$ and $g_{\mu\nu}^{ST}$ are the spin-isospin components of the g -matrix interaction.

The Kyushu g -matrix [7] is constructed from the chiral interactions with the cutoff 550 MeV. In the LF folding model, the chiral g -matrix is replaced by the LF t matrix. For a ^{12}C target, we use the phenomenological density of Ref. [55] with $r_m = 2.338$ fm.

The σ_R are determined from the S -matrices as

$$\sigma_R = \frac{\pi}{k^2} \sum_L (2L+1)(1 - |S_L|^2), \quad (26)$$

where k is a wave number and L is an angular momentum with respect to \mathbf{R} . Glauber-model calculations regard σ_R as σ_I , when the data are $\sigma_{I(\text{exp})}$. We take the same assumption.

The U_{CE} are obtained from proton and neutron densities of P and T, as shown in Eq. (21) an Eq. (22). Solving Eq. (20), one can get the S -matrices. The S -matrices yield the σ_R .

There is an empirical relation $\sigma_R = c [r_m(\text{P}) + r_m(\text{T})]^2$ between σ_R and $r_m(\text{P})$. Note that a constant c is obtained from σ_R and $r_m(\text{P})$.

D. Scaling procedure

The scaled density $\rho_{\text{scaling}}(\mathbf{r})$ is obtained from the original projectile density $\rho(\mathbf{r})$ as

$$\rho_{\text{scaling}}(\mathbf{r}) = \frac{1}{\alpha^3} \rho(\mathbf{r}/\alpha) \quad (27)$$

with a scaling factor

$$\alpha = \sqrt{\frac{\langle r^2 \rangle_{\text{scaling}}}{\langle r^2 \rangle}}. \quad (28)$$

In general, we scale the D1S-GHFB+AMP or SLy7 proton and neutron densities with Eq. (27) so as to reproduce $\sigma_{R(\text{exp})}$ under the condition that $r_{p,\text{scaling}} = r_{p(\text{exp})}$ of Refs. [4, 5]. The scaled neutron and proton radii thus uniquely determined are the experimental values.

We assume $A = 208$ for ^{nat}Pb . For $p+^{nat}\text{Pb}$ scattering, we scale the D1S-GHFB+AMP neutron density only to the scaled neutron density having $r_n(\text{PREX-II})$ by using Eq. (27), since $r_p(\text{D1S} - \text{GHFB} + \text{AMP}) = r_p(\text{PREX-II})$.

As for scattering of Na and Ar isotopes and ^{24}Mg on a ^{12}C target at around 800 MeV/u, we use the LF t -matrix folding model. In this case, we introduce a fine-tuning factor F and scale the proton and neutron densities so as to reproduce $\sigma_I(\text{exp}) = F\sigma_R(\text{LF})$ under the condition that $r_{p,\text{scaling}} = r_{p(\text{exp})}$.

We use the ESP-f of Ref. [29] for σ_R of $p+^{40}\text{Ar}$ scattering. Now, we explain the ESP-f. The fine-tuning factor f is obtained by averaging $\sigma_R(\text{exp})/\sigma_R(\text{th})$ over E_{lab} . The f $\sigma_R(\text{th})$ is scaled so as to reproduce the data, where the $\sigma_R(\text{th})$ is calculated with the Kyushu g -matrix folding model with reliable proton and neutron densities.

The g matrices include in-medium effects, but the t matrices do not. In-medium effects are negligible when $E_{\text{lab}} \geq 550$ MeV/u for the σ_R of $^{12}\text{C}+^{12}\text{C}$ scattering [56]. The scaling procedure changes the folding potential, but the scaling factor α is close to 1. Therefore, the Kyushu g -matrix folding model has almost in-medium effects at $\alpha_n = 1$; for example $\alpha_n = 0.986$ for ^{nat}Pb .

III. RESULTS

A. Determination of r_{skin}^{nat-Pb} from the reaction cross sections

Figure 3 shows E_{lab} dependence of σ_R for $p+^{nat}\text{Pb}$ scattering in $E_{\text{lab}} = 21.1 \sim 341$ MeV. We assume $A = 208$ for ^{nat}Pb . The $\sigma_R(\text{PREX-II})$ are calculated with the Kyushu g -matrix folding model with the D1S-GHFB+AMP neutron density scaled to $r_n^{208}(\text{PREX-II})$, where $r_p^{208}(\text{D1S}) = r_p^{208}(\text{PREX-II})$. The $\sigma_R(\text{PREX-II})$ almost reproduce the central value of the data [10–16] for each E_{lab} .

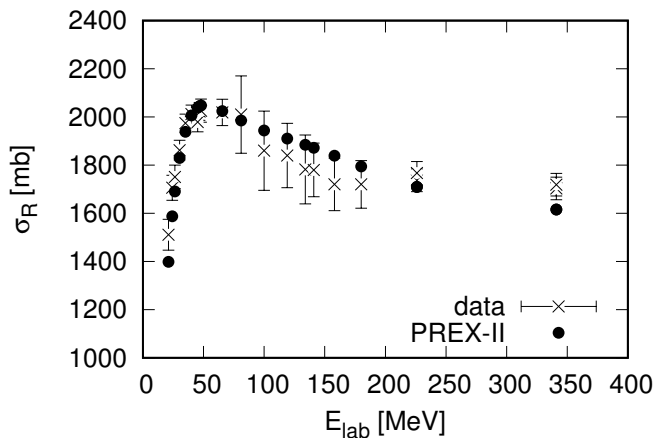


FIG. 3. E_{lab} dependence of σ_R for $p+^{nat}\text{Pb}$ scattering. Closed circles denote $\sigma_R(\text{PREX-II})$. The data are taken from Ref. [10–16]. Note that the cross sections calculated with the scaled densities are not shown, since the cross sections with the scaled densities reproduce the data.

Scaling the PREX-II neutron density for ^{nat}Pb to the data [10–16] in $E_{\text{lab}} = 21.1 \sim 341$ MeV, we can obtain $r_{\text{skin}}^{nat-Pb} = 0.271 \pm 0.008$ fm. The value agrees with $r_{\text{skin}}^{208Pb}(\text{PREX-II})$. The values of r_{skin} and $r_m(\sigma_R)$ are shown in Table III. The detailed procedure of the scaling will be explained in Sec. III B.

TABLE III. Values of $r_m(\sigma_R)$, $r_p, r_n, r_{\text{skin}}$ for ^{nat}Pb based on proton scattering, where we assume $A = 208$. The radii are shown in units of fm.

A	r_{skin}	error	$r_m(\sigma_R)$	error	r_n	error	r_p
208	0.271	0.008	5.610	0.005	5.715	0.008	5.444

In Refs. [6, 29], we extracted $r_{\text{skin}}^{208} = 0.278 \pm 0.035$ fm from σ_R on $p+^{208}\text{Pb}$ in $20 \leq E_{\text{lab}} \leq 180$ MeV. Our present value $r_{\text{skin}} = 0.271 \pm 0.008$ fm for ^{nat}Pb agrees with our previous value $r_{\text{skin}}^{208} = 0.278 \pm 0.035$ fm for ^{208}Pb .

B. Determination of r_{skin} and r_m for ^{159}Tb

We extract r_{skin} and $r_m(\sigma_R)$ from the data σ_R [17] in $20 \leq E_{\text{lab}} \leq 47.5$ MeV, using the Kyushu g -matrix folding model with the D1S-GHFB densities. ^{159}Tb is a deformed nucleus; the deformation parameter β_2 calculated with D1S-GHFB is 0.309.

Figure 4 shows our σ_R based on the Kyushu g -matrix folding model with the D1S-GHFB densities and the data [17]. The Kyushu g -matrix folding model (open circles) almost reproduces the central value of the data for each E_{lab} .

Taking the scaling procedure of Sec. II D for the D1S-GHFB proton and neutron densities, i.e., for each E_{lab} , we scale $r_n(E_{\text{lab}})$ so as to $\sigma_R(\text{scaled}) = \sigma_R(\text{exp})$ under $r_{p,\text{scaled}} = r_p(\text{exp})$ of electron scattering [5]. We next take a weighted average of $r_n(E_{\text{lab}})$ over E_{lab} . The resultant value is $r_n(\sigma_R)$. We finally obtain $r_{\text{skin}} = r_n(\sigma_R) - r_p(\text{exp})$ and $r_m(\sigma_R)$; note that $A r_m(\sigma_R)^2 = N r_n(\sigma_R)^2 + Z r_p(\text{exp})^2$. Our results based on the scaled proton and neutron densities are shown in Table IV.

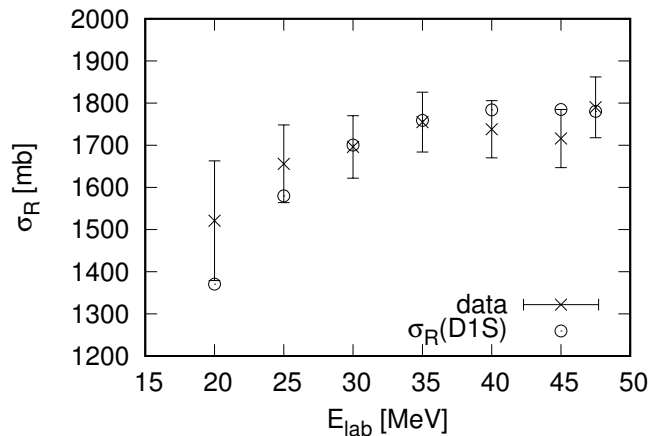


FIG. 4. E_{lab} dependence of σ_R for $p+^{159}\text{Tb}$ scattering. Open circles stand for the σ_R calculated with the Kyushu g -matrix folding model with the D1S-GHFB (original) densities. The data are taken from Refs. [17]. Note that the cross sections calculated with the scaled densities are not shown, since the cross sections with the scaled densities reproduce the data.

TABLE IV. Values of $r_m(\sigma_R)$, $r_p, r_n, r_{\text{skin}}$ for ^{159}Tb . The radii are shown in units of fm.

A	r_{skin}	error	$r_m(\sigma_R)$	error	r_n	error	r_p
159	0.273	0.073	5.160	0.044	5.270	0.073	4.997

C. Mg isotopes

We first explain “D1S-GHFB+AMP” in the spherical limit”. The D1S Hamiltonian is diagonalized in the space

spanned by the spherical Harmonic oscillator bases. Using the wave function thus obtained, we calculate the matter radius.

In Fig. 5, the experimental matter radii $r_m(\sigma_I)$ of Ref. [19] are compared with the experimental matter radii $r_m(\sigma_R)$ of Ref. [25] for $^{24-38}\text{Mg}$. The theoretical deformed matter radii $r_m(\text{deformed})$ (the solid line) calculated with DIS-GHFB+AMP are closer to the experimental $r_m(\sigma_R)$, whereas the theoretical $r_m(\text{spherical})$ (the dashed line) calculated with DIS-GHFB in the spherical limit are near the central value of the experimental $r_m(\sigma_I)$. The experimental $r_m(\sigma_I)$ of Ref. [19] yield matter radii in the spherical limit. For $^{24-38}\text{Mg}$, the experimental $r_m(\sigma_R)$ of Ref. [25] include effects of deformation.

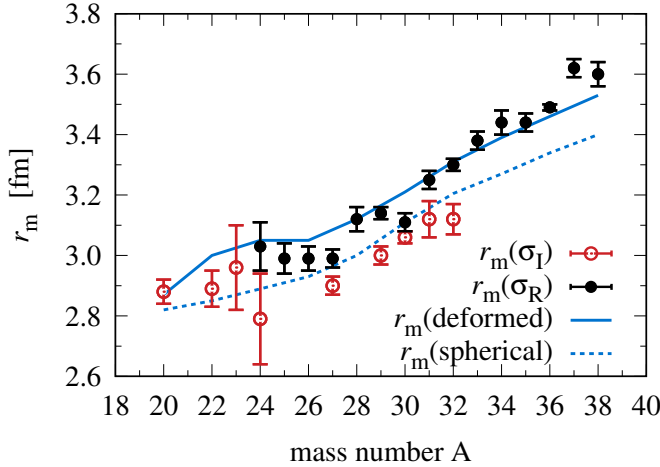


FIG. 5. A dependence of r_m for Mg isotopes. Open circles with error-bar denote the experimental $r_m(\sigma_I)$ of Ref. [19] and closer circles with error-bar correspond to the experimental $r_m(\sigma_R)$ of Ref. [25]. For even-even Mg isotopes, the solid line stands for the theoretical $r_m(\text{deformed})$ calculated with DIS-GHFB+AMP, whereas the dashed line corresponds to the theoretical $r_m(\text{spherical})$ calculated with DIS-GHFB in the spherical limit.

For ^{24}Mg , the $r_m(\sigma_I) = 2.79 \pm 0.15$ fm of Ref. [19] and the $r_m(\sigma_R) = 3.03 \pm 0.08$ fm of Ref. [25] were extracted from $^{24}\text{Mg}+^{12}\text{C}$ scattering, Using $\sigma_{I,R}(\text{exp}) = c[r_m(^{24}\text{Mg}) + r_m(^{12}\text{C})]^2$ for a constant c , we can obtain $(\sigma_R - \sigma_I)/\sigma_R = 0.087$. For a ^{12}C target, we use the phenomenological density of Ref. [55] with $r_m(^{12}\text{C}) = 2.338$ fm.

As a further analysis, we consider whether $(\sigma_R - \sigma_I)/\sigma_R = 0.087$ for $^{24}\text{Mg}+^{12}\text{C}$ scattering stems from effects of deformation only. In Eq. (3), the σ_{inela} are the total inelastic cross sections. When a projectile (P) has large deformation, the σ_{inela} are not negligible compared with σ_I . There is an empirical formula between σ_R and $r_m(\text{P})$:

$$\sigma_R = c [r_m(\text{P}) + r_m(\text{T})]^2. \quad (29)$$

There is an approximation equation having β_2 for $r_m(\text{P})$:

$$r_m^2(\text{P}) = r_{m,0}^2(\text{P}) \left[1 + \frac{5\beta_2^2}{4\pi} \right] = r_{m,0}^2(\text{P}) [1 + x], \quad (30)$$

where $r_{m,0}$ is the matter radius in the spherical limit and $r_{m,0} = 2.929$ fm for $\beta_2 = 0.48$ calculated with DIS-GHFB+AMP. Using the two equations, we can obtain

$$\sigma_R = c [r_m(\text{P}) + r_m(\text{T})]^2, \quad (31)$$

$$\sigma_I = c [r_{m,0}(\text{P}) + r_m(\text{T})]^2, \quad (32)$$

$$\sigma_{\text{inel}} = 2cx[(1+x)r_{m,0}(\text{P})^2 + r_{m,0}(\text{P})r_m(\text{T})]. \quad (33)$$

The σ_{inel} tend to zero in the limit of $\beta_2 = 0$ ($x = 0$). The σ_I yield an experimental matter radius in the spherical limit.

In Fig. 5, the theoretical deformed matter radii $r_m(\text{deformed})$ (the solid line) calculated with DIS-GHFB+AMP are close to the experimental $r_m(\sigma_R)$, but the theoretical $r_m(\text{spherical})$ (the dashed line) calculated with DIS-GHFB in the spherical limit overshoots the central value of the experimental $r_m(\sigma_I) = 2.79 \pm 0.15$ fm of Ref. [19]. Eventually, the value of $(\sigma_R - \sigma_I)/\sigma_R$ is 0.037, when we consider effects of deformation only.

The $(\sigma_R - \sigma_I)/\sigma_R$ is 0.037 is smaller than the $(\sigma_R - \sigma_I)/\sigma_R = 0.087$ mentioned above. The difference comes from the fact that the $r_m(\sigma_I) = 2.79 \pm 0.15$ fm of Ref. [19] is too small compared with the $r_{m,0}(\text{P}) = 2.929$ fm obtained by Eq. (30). In Fig. 5, in addition, the $r_m(\sigma_I)$ for ^{23}Mg is larger than that for ^{24}Mg . These facts indicate that the central value of $r_m(\sigma_I) = 2.79 \pm 0.15$ fm for ^{24}Mg is too small. The $r_m(\sigma_I) = 2.79 \pm 0.15$ fm for ^{24}Mg may come from a fluctuation. In any case, σ_I experiments are expected in order to obtain $r_m(\sigma_I)$.

It should be noted that DIS-GHFB+AMP in the spherical limit yields $r_m(\text{spherical}) = 2.925$ fm. The $r_{m,0}(\text{P}) = 2.929$ fm obtained by Eq. (30) agrees with $r_m(\text{spherical}) = 2.925$ fm. This indicates that Eq. (30) is good.

The r_{skin} values of Table V are calculated from the $r_m(\sigma_R)$ of Ref. [25] with the $r_p(\text{exp})$ determined from the charge radii [5].

TABLE V. Our results of r_m , r_n , r_{skin} , r_p for Mg isotopes. The $r_p(\text{exp})$ are determined from the charge radii [5]. The $r_m(\sigma_R)$ are taken from Ref. [25]. The radii are shown in units of fm.

A	r_{skin}	error	$r_m(\sigma_R)$	error	$r_n(\text{exp})$	error	$r_p(\text{exp})$
24	0.17	0.15	3.03	0.08	3.11	0.15	2.943
25	0.14	0.09	2.99	0.05	3.06	0.09	2.915
26	0.13	0.07	2.99	0.04	3.05	0.07	2.922

D. Na isotopes

As for $^{21,23}\text{Na}$, SLy7 yields better agreement with the $r_m(\sigma_I)$ of Refs. [18, 22] than DIS-GHFB do. This indicates that SLy is better than DIS-GHFB for the scaling procedure. We then use SLy7 for the scaling procedure.

Following the Glauber-model calculations of Ref. [23], we introduce a fine-tuning factor F in our folding model. In this case, the F is determined so as to reproduce the central value of $r_m(\sigma_I) = 2.79 \pm 0.15$ fm [18] for $^{24}\text{Mg}+^{12}\text{C}$ scattering

in which the SLy7 densities are used for ^{24}Mg . The resulting value is $F = 0.955$.

Figure 6 shows A dependence of σ_I for Na isotopes. The LF t -matrix folding model with the SLy7 densities overshoots the data [18]. A dependence of the data [18, 22] is not natural at $A = 22$. The $F\sigma_R$ calculated with the LF t -matrix folding model with $F = 0.955$ are slightly larger than the data. The $F\sigma_R$ are scaled with the scaling procedure of Sec. II D and Sec. III B. The resultant values $r_m(\sigma_I)$ are tabulated in Table VI.

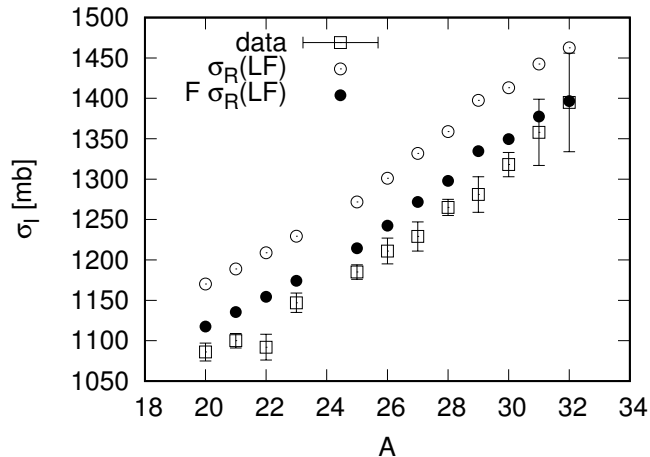


FIG. 6. A dependence of σ_I for Na isotopes. Open circles stand for the results of the LF t -matrix folding model with the SLy7 densities. Closed circles correspond to the $F\sigma_R(\text{LF})$ with the SLy7 densities with $F = 0.955$. The data are taken from Refs. [18, 22]. Note that the cross sections calculated with the scaled densities are not shown, since the cross sections with the scaled densities reproduce the data.

TABLE VI. Our values on $r_m(\sigma_I)$ for Na isotopes based on σ_I . The $r_p(\text{exp})$ are determined from the charge radii [5]. The radii are shown in units of fm.

A	r_{skin}	error	$r_m(\sigma_I)$	error	$r_n(\text{exp})$	error	$r_p(\text{exp})$
20	-0.231	0.060	2.749	0.026	2.620	0.060	2.850
21	-0.288	0.046	2.762	0.021	2.607	0.046	2.896
22	-0.293	0.078	2.725	0.037	2.575	0.078	2.868
23	-0.086	0.052	2.834	0.027	2.793	0.052	2.879
25	0.039	0.035	2.887	0.020	2.904	0.035	2.865
26	0.075	0.059	2.927	0.035	2.958	0.059	2.883
27	0.070	0.064	2.949	0.039	2.977	0.064	2.907
28	0.133	0.034	3.017	0.021	3.069	0.034	2.936
29	0.101	0.073	3.055	0.046	3.093	0.073	2.992
30	0.144	0.048	3.112	0.031	3.164	0.048	3.020
31	0.166	0.125	3.184	0.083	3.242	0.125	3.076
32			3.255	0.121			

Figure 7 show our $r_m(\sigma_I)$, the $r_m(\sigma_{\text{Suzuki}})$ of Refs. [18, 22], the $r_m(\text{SLy7})$ for Na isotopes as a function of A . Our $r_m(\sigma_I)$ are consistent with the $r_m(\sigma_{\text{Suzuki}})$. The $r_m(\text{SLy7})$

are parallel to our $r_m(\sigma_I)$ and have natural A dependence, i.e., $r_m(\text{SLy7}) = 1.1263A^{1/3} - 0.3243$ with good accuracy. We may say that Sly7 is a good EoS for Na isotopes.

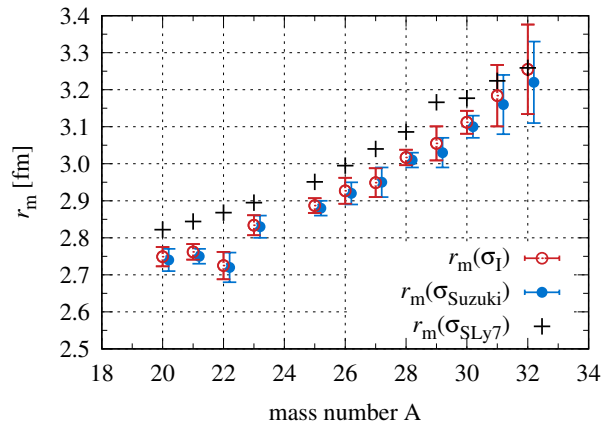


FIG. 7. A dependence of our $r_m(\sigma_I)$. [18, 22], $r_m(\sigma_{\text{Suzuki}})$, $r_m(\sigma_{\text{SLy7}})$ for Na isotopes. Open circles with error-bar stand for our $r_m(\sigma_I)$, whereas closed circles with error-bar correspond to the $r_m(\sigma_{\text{Suzuki}})$. [18, 22]. The symbol '+' denote $r_m(\sigma_{\text{SLy7}})$.

As shown in Fig. 8, our values $r_m(\sigma_I)$ of Table VI are compared with those of Refs. [19, 22] for $^{21,23,25,27,29,31}\text{Na}$. Our values $r_m(\sigma_I)$ agree with those of Refs. [19, 22].

Zhang *et al.* measured σ_R for $^{21,23}\text{Na}+^{12}\text{C}$ scattering at around 30 MeV/u [21]. Using the Kyushu g -matrix with the Sly7 proton and neutron densities and the scaling procedure of Eq. (27), we extracted $r_m(\sigma_R) = 2.976 \pm 0.171$ fm (2.928 ± 0.125 fm) from the σ_R for ^{21}Na (^{23}Na); see Table VII.

TABLE VII. Values on $r_m(\sigma_R)$, $r_p, r_n, r_{\text{skin}}$ for $^{21,23}\text{Na}$. The radii are shown in units of fm.

A	r_{skin}	error	$r_m(\sigma_R)$	error	r_n	error	r_p
21	0.283	0.334	2.976	0.171	3.121	0.334	2.838
23	0.094	0.232	2.928	0.125	2.972	0.232	2.879

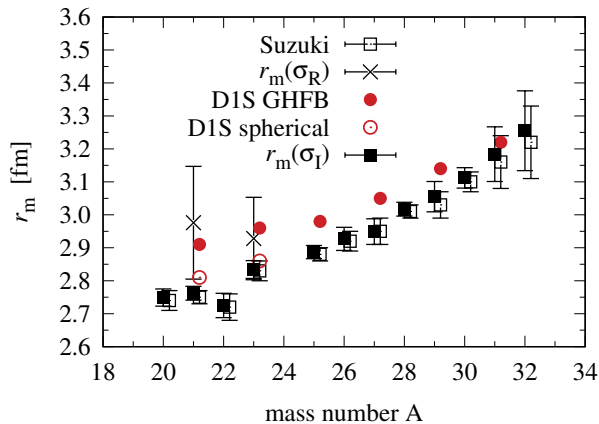


FIG. 8. A dependence of r_m for Na isotopes. Closed circles denote the r_m of D1S-GHFB, and open circles correspond to the r_m of D1S-GHFB in spherical limit. Closed squares with error-bar correspond to our values $r_m(\sigma_I)$, while open squares with error-bar do to the $r_m(\sigma_I)$ of Refs. [19, 22]. Crosses with error-bar show $r_m(\sigma_R) = 2.976 \pm 0.171$ fm (2.928 ± 0.125 fm) for ^{21}Na (^{23}Na).

As shown in Fig. 8, for $^{21,23}\text{Na}$, the central values of $r_m(\sigma_R)$ are close to the $r_m(\text{D1S})$ (the results of D1S-GHFB), whereas the $r_m(\text{D1S} - \text{spherical})$ (the results of D1S-GHFB in the spherical limit) are near our values $r_m(\sigma_I)$ and those of Refs. [19, 22].

For $^{21,23}\text{Na}$, the fact that the $r_m(\text{D1S} - \text{spherical})$ are close to our values $r_m(\sigma_I)$ indicates that our values $r_m(\sigma_I)$ and the $r_m(\sigma_I)$ of Refs. [19, 22] are matter radii in spherical limit. Meanwhile, our $r_m(\sigma_R)$ include effects of deformation.

For $^{24-38}\text{Mg}$, the $r_m(\text{D1S})$ almost agree with the $r_m(\sigma_R)$ [25] including effects of deformation. This agreement happens for $^{21,23,25,27,29,31}\text{Na}$. For $^{21,23,25,27,29,31}\text{Na}$, D1S-GHFB yields $\beta_2 = 0.406, 0.412, 0.291, 0.258, 0.201, 0.133$ for $^{21,23,25,27,29,31}\text{Na}$, respectively.

E. Ar isotopes

As for $^{32,34,36,38,40}\text{Ar}$, SLy7 yields better agreement with the $r_m(\sigma_I)$ of Ref. [23] than D1S-GHFB+AMP. As the scaling procedure, SLy is better than D1S-GHFB+AMP. This is the reason why we use SLy7.

At $E_{\text{lab}} = 950$ MeV/u, there is no σ_I between Mg isotopes and Ar isotopes. Following Ref. [23], we introduce a fine-tuning factor F . In this case, the F is determined so as to reproduce the central value of $r_m(\sigma_I) = 2.79 \pm 0.15$ fm [18] for ^{24}Mg . The resulting value is $F = 0.955$, where the data $\sigma_I(\text{exp}) = 1136 \pm 72$ mb [18, 19] and the the cross sections calculated with the SLy7 proton and neutron densities is $\sigma_I = 1252$ mb for $^{24}\text{Mg} + ^{12}\text{C}$ scattering. The resulting value $F = 0.955$ is used also for $^{32-40}\text{Ar} + ^{12}\text{C}$ scattering.

Figure 9 shows σ_I as a function of A . The LF t -matrix folding model with the SLy7 densities overestimates the data [23]. The $F\sigma_I(\text{LF})$ monotonically increase as a function of A , whereas the data [23] have a depression in $^{37,38}\text{Ar}$. The de-

pression in $^{37,38}\text{Ar}$ may be a fluctuation of the data. The σ_I experiments are expected for Ar isotopes.

The $F\sigma_I$ calculated with the LF t -matrix folding model with F satisfies $cF [r_m(\text{SLy7}) + r_m(\text{T})]^2$. Except for $A = 37, 38$, the c hardly depend on A .

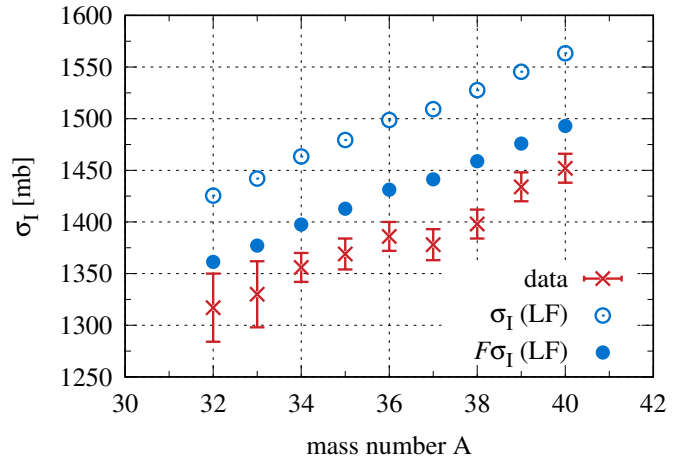


FIG. 9. A dependence of σ_I for Ar isotopes. Open circles stand for the results of the LF t -matrix folding model with the SLy7 densities. Closed circles correspond to the $F\sigma_I(\text{LF})$ with the SLy7 densities with $F = 0.955$. The data is taken from Refs. [23]. Note that the cross sections calculated with the scaled densities are not shown, since the cross sections with the scaled densities reproduce the data.

The $F\sigma_R$ calculated with the LF t -matrix folding model with $F = 0.955$ are slightly larger than the data. The $F\sigma_R$ are scaled with the scaling procedure of Sec. IID and Sec. III B. The resultant values $r_m(\sigma_I)$ are tabulated in Table VIII.

Our values $r_m(\sigma_I)$ are compared with the $r_m(\text{Ozawa})$ of Ref. [23], as shown in Fig. 10. Our results are consistent with those of Ref. [23]. Both our $r_m(\sigma_I)$ and $r_m(\text{Ozawa})$ have a depression in $^{37,38}\text{Ar}$. SLy7 and D1S do not yield the depression. The reason why our $r_m(\sigma_I)$ and $r_m(\text{Ozawa})$ are smaller than the $r_m(\sigma_I)$ of the neighborhood nuclei stems from the fact that the data σ_I of Ref. [23] are smaller for $^{37,38}\text{Ar}$.

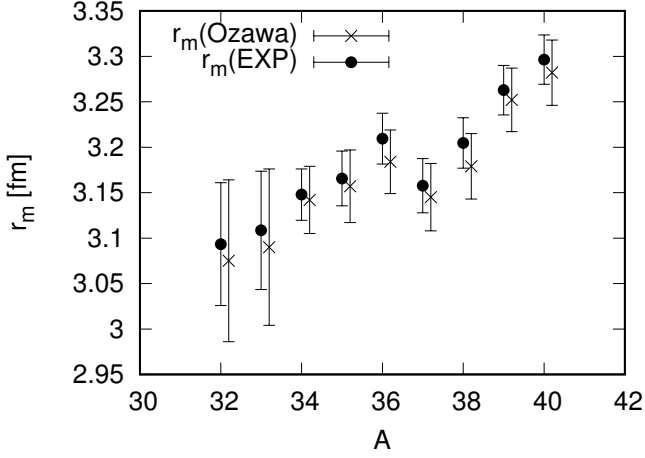


FIG. 10. A dependence of $r_m(\sigma_I)$ for Ar isotopes. Closed circles with error-bar correspond to our values, while crosses with error-bar does to those of Ref. [23].

Figure 11 shows our results on proton skin thickness $r_{\text{skin,p}}$ for $^{32-40}\text{Ar}$. There is a bump at $A = 37, 38$. This is related to the fact that the central values of $\sigma_I(\text{exp})$ are slightly smaller than those of the neighborhood nuclei. If we take the upper-bound values of the data $\sigma_I(\text{exp})$ for $A = 37, 38$ in Fig. 9, we obtain Fig. 12 in which the bump almost disappears. The bump comes from the depression in $^{37,38}\text{Ar}$ shown in Fig. 9, The depression in $^{37,38}\text{Ar}$ may be a fluctuation of the data. Our final results are the $r_{\text{skin,p}}$ of Fig. 11, since it is not easy to avoid the fluctuation. The re-measurements are expected.

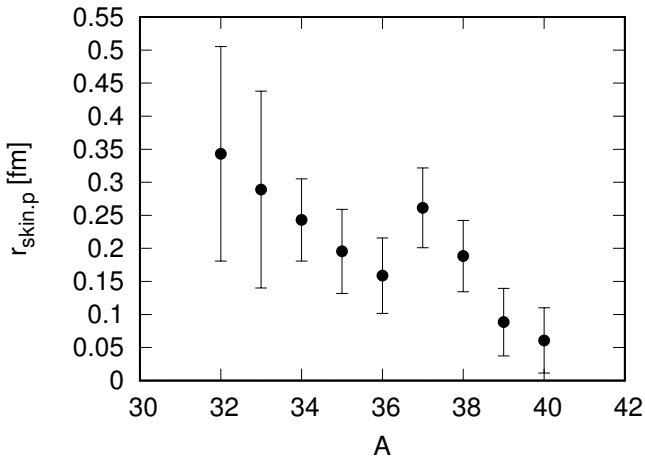


FIG. 11. A dependence of $r_{\text{skin,p}}$ for $^{32-40}\text{Ar}$.

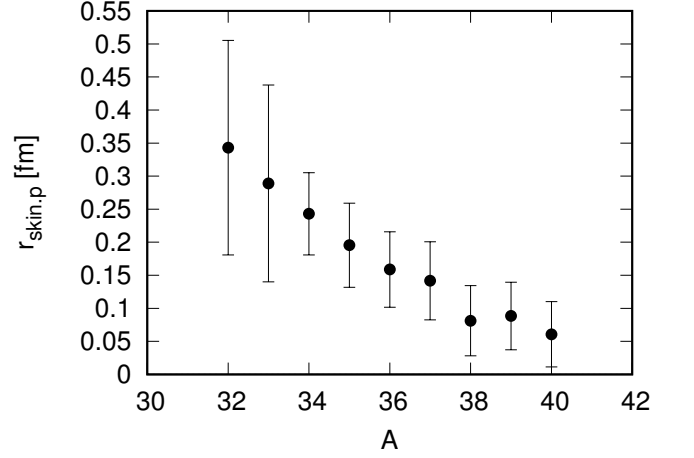


FIG. 12. A dependence of $r_{\text{skin,p}}$ for $^{32-40}\text{Ar}$ in which the upper-bound values are taken for $A = 37, 38$.

Our results are tabulated in Table VIII. Our values $r_m(\sigma_I)$ are consistent with those of Ref. [23].

TABLE VIII. Values on $r_p, r_m(\sigma_I), r_n, r_{\text{skin,p}}$ for Ar isotopes based on σ_I . The radii are shown in units of fm.

A	r_{skin}	error	$r_m(\sigma_I)$	error	r_n	error	r_p
32	0.343	0.163	3.093	0.068	2.896	0.163	3.2387
33	0.289	0.149	3.109	0.065	2.948	0.149	3.2366
34	0.243	0.062	3.148	0.028	3.017	0.062	3.2599
35	0.195	0.064	3.166	0.030	3.064	0.064	3.2590
36	0.159	0.057	3.209	0.028	3.129	0.057	3.2878
37	0.261	0.060	3.158	0.030	3.028	0.060	3.2891
38	0.188	0.054	3.205	0.028	3.114	0.054	3.3024
39	0.088	0.051	3.263	0.027	3.222	0.051	3.3101
40	0.061	0.049	3.296	0.027	3.269	0.049	3.3297

F. $p+^{40}\text{Ar}$ scattering

There is no data on σ_R for $^{32-39}\text{Ar}$. Now, we extract $r_m(\sigma_R)$ from $\sigma_R(\text{exp})$ [39] for $p+^{40}\text{Ar}$ scattering, using the Kyushu g -matrix folding model with the Sly7 proton and neutron densities.

Figure 13 shows our values on σ_R and the data [39]. The Kyushu g -matrix folding model with the SLy7 densities almost agrees with the data [39]. We then introduce a fine-tuning factor f . We use the reliable ESP-f of Ref. [29] in order to determine f . The fine-tuning factor f is obtained by averaging $\sigma_R(\text{exp})/\sigma_R(\text{th})$ over E_{lab} . The resulting value is $f = 1.0327$. After the scaling procedure based on ESP-f, we obtain $r_m(\sigma_R)$, as shown in Table IX. The $r_m(\sigma_R)$ is larger than $r_m(\sigma_I)$, as shown in Table VIII.

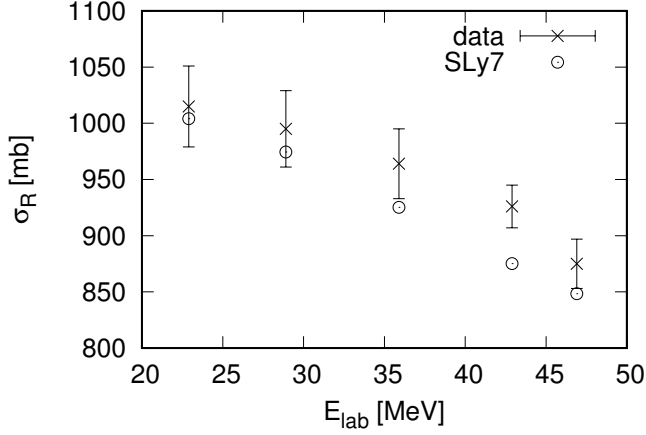


FIG. 13. E_{lab} dependence of σ_{R} for $p+^{40}\text{Ar}$ scattering. Open circles stand for results of the Kyushu g -matrix folding model with the SLy7 densities. The data is taken from Refs. [39]. Note that the cross sections calculated with the scaled densities are not shown, since the cross sections with the scaled densities reproduce the data.

TABLE IX. Values on $r_{\text{m}}(\sigma_{\text{R}})$, $r_{\text{p}}, r_{\text{n}}, r_{\text{skin}}$ for ^{40}Ar based on proton scattering. The radii are shown in units of fm.

A	r_{skin}	error	$r_{\text{m}}(\sigma_{\text{R}})$	error	r_{n}	error	r_{p}
40	0.094	0.054	3.381	0.030	3.423	0.054	3.3297

Figure 14 show A dependence of the $r_{\text{m}}(\sigma_{\text{R}})$ of Table IX, the $r_{\text{m}}(\sigma_{\text{I}})$ of Table VIII, the $r_{\text{m}}(\sigma_{\text{I}})$ of Ref. [23]. These experimental values are compared with the theoretical matter radii, $r_{\text{m}}(\text{AMP})$ ($r_{\text{m}}(\text{deformed})$) and $r_{\text{m}}(\text{spherical})$, for $^{32,34,36,38,40}\text{Ar}$, where the $r_{\text{m}}(\text{AMP})$ are the results calculated with D1S-GHFB+AMP, whereas $r_{\text{m}}(\text{spherical})$ corresponds to D1S-GHFB+AMP in the spherical limit. Note that D1S-GHFB+AMP yields $\beta_2 = 0.244, 0.225, 0.219, 0.149, 0.203$ for $^{32,34,36,38,40}\text{Ar}$, respectively. Note that the AMP calculations are very difficult for odd nuclei; see Ref. [57] for the difficulty. As for ^{38}Ar , the β_2 is smallest, because of $N = 20$ (closed shell).

For ^{40}Ar , the $r_{\text{m}}(\text{AMP})$ and the $r_{\text{m}}(\text{spherical})$ reproduce our $r_{\text{m}}(\sigma_{\text{R};\text{p scattering}})$ (Symbol “+” with an error-bar) extracted from $p+^{40}\text{Ar}$ scattering within the error-bar of $r_{\text{m}}(\sigma_{\text{R};\text{p scattering}})$. This indicates that the $r_{\text{m}}(\sigma_{\text{R};\text{p scattering}})$ includes effects of deformation, although the effects are small. Our value $r_{\text{m}}(\sigma_{\text{I}})$ for ^{40}Ar is below $r_{\text{m}}(\text{spherical})$, indicating that our value $r_{\text{m}}(\sigma_{\text{I}})$ does not includes effects of deformation.

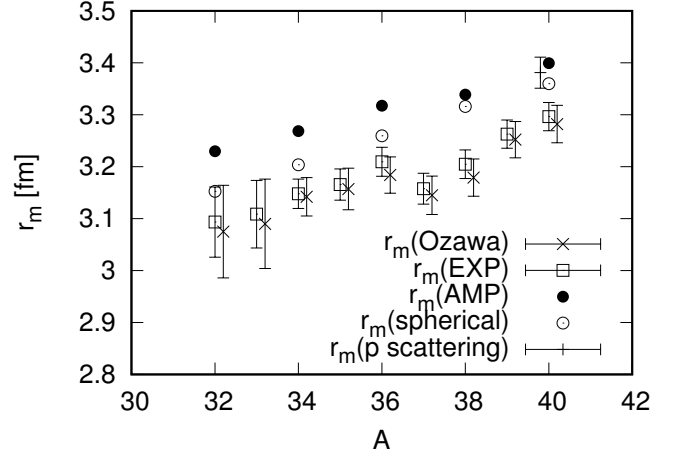


FIG. 14. A dependence of r_{m} for Ar isotopes. Closed circles denote the r_{m} of . D1S-GHFB+AMP, whereas open circles correspond to the r_{m} of D1S-GHFB+AMP in spherical limit Squares with error-bar denote our values $r_{\text{m}}(\sigma_{\text{I}})$, while crosses with error-bar correspond to the $r_{\text{m}}(\text{Ozawa})$ of Ref. [23]. Symbol “+” with an error-bar shows $r_{\text{m}}(\sigma_{\text{R};\text{p scattering}})$.

IV. SUMMARY

We have extracted the neutron skin thickness $r_{\text{skin}} = 0.271 \pm 0.008$ fm for ^{nat}Pb from σ_{R} of $p+^{nat}\text{Pb}$ scattering in $21 \lesssim E_{\text{lab}} \lesssim 341$ MeV, using the chiral (Kyushu) g -matrix folding model, where we assume $A = 208$ for ^{nat}Pb . The chiral (Kyushu) g -matrix folding model having r_{p} (PREX-II) and r_{m} (PREX-II) reproduce the data in $21 \lesssim E_{\text{lab}} \lesssim 341$ MeV. This indicates that the chiral (Kyushu) g -matrix folding model is reliable there. The skin value for ^{nat}Pb agrees with $r_{\text{skin}}^{208\text{Pb}}(\text{PREX-II}) = 0.283 \pm 0.071$ fm for ^{208}Pb . Meanwhile, in Refs. [6, 29], we extracted $r_{\text{skin}}^{208\text{Pb}} = 0.278 \pm 0.035$ fm from σ_{R} on $p+^{208}\text{Pb}$ in $20 \lesssim E_{\text{lab}} \lesssim 180$ MeV. Our present value $r_{\text{skin}}^{nat} = 0.271 \pm 0.008$ fm of ^{nat}Pb agrees with our previous value $r_{\text{skin}}^{208\text{Pb}} = 0.278 \pm 0.035$ fm of ^{208}Pb . Prediction A may be true, where prediction A is that the skin values for $^{208,207,206,204}\text{Pb}$ are almost constant as a function of A , as mentioned in Sec. I.

For ^{159}Tb , our results are $r_{\text{m}} = 5.160 \pm 0.044$ fm and $r_{\text{skin}} = 0.273 \pm 0.073$ fm; note that D1S-GHFB shows $\beta_2 = 0.309$.

$$r_{\text{m}}^2 = r_{\text{m},0}^2 \left[1 + \frac{5\beta_2^2}{4\pi} \right] = r_{\text{m},0}^2 \quad (34)$$

where $r_{\text{m},0}$ is the matter radius in the spherical limit. Using Eq. (34), we can get $r_{\text{m},0} = 5.065 \pm 0.044$ fm and $r_{\text{skin},0} = 0.114 \pm 0.074$ fm in the spherical limit. Effects of deformation are thus large for r_{skin}

We have determined matter radii $r_{\text{m}}(\sigma_{\text{R}})$ and $r_{\text{skin}}(\sigma_{\text{R}})$ for ^{40}Ar and $r_{\text{m}}(\sigma_{\text{I}})$ and $r_{\text{skin}}(\sigma_{\text{R}})$ for $^{20-32}\text{Na}$, $^{32-40}\text{Ar}$; see Tables VI, VII, VIII, IX. We have used the Kyushu g -matrix folding model for low and intermediate energies and the LF t -matrix folding model for high energies.

As for ^{24}Mg , our value $r_m(\sigma_R) = 3.03 \pm 0.08$ fm [25] includes effects of deformation, whereas the $r_m(\sigma_I) = 2.79 \pm 0.15$ fm [22] does not.

As for even-even Mg isotopes, we have used D1S-GHFB+AMP and its spherical limit in order to find whether the nucleus we consider includes effects of deformation or not. This analyses show that the $r_m(\sigma_I)$ of Ref [19] for $^{20,22,23,27,29-32}\text{Mg}$ yield matter radii in the spherical limit, whereas the $r_m(\sigma_R)$ for $^{24-38}\text{Mg}$ of Ref. [25] include effects of deformation.

As shown in Fig. 7, our $r_m(\sigma_I)$ are consistent with the $r_m(\sigma_{\text{Suzuki}})$ of Ref. [18] for $^{20-23,25-32}\text{Na}$. Our $r_m(\sigma_I)$ and the $r_m(\sigma_{\text{Suzuki}})$ are, however, the matter radii from measured σ_I . Our $r_m(\sigma_I)$ and the $r_m(\sigma_{\text{Suzuki}})$ should be compared with matter radii $r_m(\sigma_R)$ determined from σ_R , when σ_R are available. This is because β_2 calculated with D1S-GHFB are large for $^{21,23}\text{Na}$; namely $\beta_2 = 0.406, 0.412$ for $^{21,23}\text{Na}$, respectively.

Zhang *et al.* measured reaction cross sections σ_R for $^{21,23}\text{Na}+^{12}\text{C}$ scattering at around 30 MeV/u [21]. Using the Kyushu g -matrix with the Sly7 proton and neutron densities and the scaling procedure of Sec. II D and Sec. III B., we extracted $r_m(\sigma_R) = 2.976 \pm 0.171$ fm (2.928 ± 0.125 fm) from the σ_R for ^{21}Na (^{23}Na).

For $^{21,23}\text{Na}$, our values $r_n(\sigma_R)$ include effects of deformation, but our values $r_n(\sigma_I)$ do not. For Na isotopes, our $r_n(\sigma_R)$ and our $r_n(\sigma_I)$, are shown together with $r_p(\text{exp})$ in Fig. 15. We find that effects of deformation on r_n are not negligible.

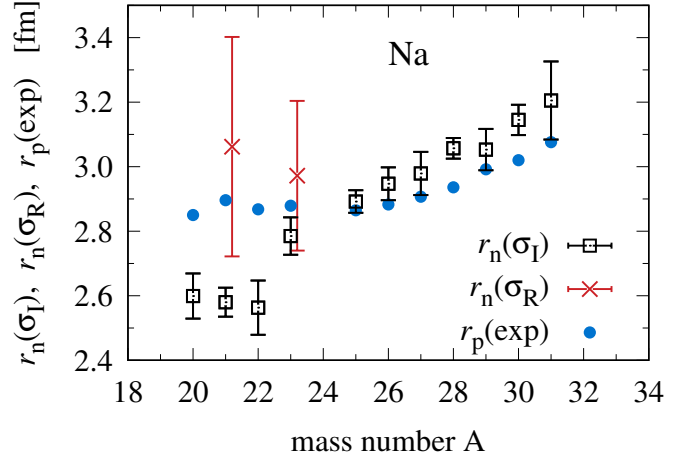


FIG. 15. A dependence of the $r_n(\sigma_I)$, the $r_n(\sigma_R)$, the $r_p(\text{exp})$ for Na isotopes. Squares with error-bar denote our values for $r_n(\sigma_I)$, while circles with error-bar correspond to the $r_p(\text{exp})$ determined from the charge radii [5]. Crosses with error-bar show our $r_n(\sigma_R) = 2.976 \pm 0.171$ fm (2.928 ± 0.125 fm) for ^{21}Na (^{23}Na).

As for Ar isotopes, our results $r_m(\sigma_I)$ are consistent with those of Ref. [23] for $^{32-40}\text{Ar}$. We extract $r_m(\sigma_R)$ from the data [39] on $\sigma_R(\text{exp})$ for $p+^{40}\text{Ar}$ scattering, using the Kyushu g -matrix folding model with the Sly7 densities in which the scaling procedure (ESP-f) of Ref. [29] is used. For ^{40}Ar , our value $r_m(\sigma_R)$ is larger than our values $r_m(\sigma_I)$. The former value includes effects of deformation, but the latter value does not.

ACKNOWLEDGEMENTS

We thank Toyokawa for his comments.

Appendix A: Definitions of quantities

The explicit forms of $\delta_0^{(\alpha)}(R, s)$ and $\rho_1^{(\alpha)}(R, s)$ are

$$\begin{aligned} \delta_0^{(\alpha)}(R, s) &= \frac{1}{2} \int_{-1}^{+1} d\omega \frac{g_{\text{LS}, p\alpha}^{\text{EX}}(s; \rho_\alpha)}{x} \\ &\times \left\{ \frac{3}{k_F^{(\alpha)}(x)s} j_1(k_F^{(\alpha)}(x)s) \frac{d}{dx} \rho_\alpha(x) \right|_{x=\sqrt{R^2+s^2/4+Rsw}} \\ &+ s \rho_\alpha(x) \frac{d}{dx} k_F^{(\alpha)}(x) \Big|_{x=\sqrt{R^2+s^2/4+Rsw}} \\ &\times \frac{d}{dy} \left[\frac{3}{y} j_1(y) \right] \Big|_{y=k_F^{(\alpha)}(x)s} \right\}, \end{aligned} \quad (\text{A1})$$

and

$$\begin{aligned} \rho_1^{(\alpha)}(R, s) &= \frac{1}{2} \int_{-1}^{+1} d\omega \omega g_{\text{LS}, p\alpha}^{\text{EX}}(s; \rho_\alpha) \frac{3}{k_F^{(\alpha)}(x)s} \\ &\times j_1(k_F^{(\alpha)}(x)s) \rho_\alpha(y) \Big|_{y=\sqrt{R^2+s^2/4+Rsw}}, \end{aligned} \quad (\text{A2})$$

- [1] C. J. Horowitz, S. J. Pollock, P. A. Souder, and R. Michaels, Parity violating measurements of neutron densities, *Phys. Rev. C* **63**, 025501 (2001).
- [2] D. Adhikari et al. (PREX), Accurate Determination of the Neutron Skin Thickness of ^{208}Pb through Parity-Violation in Electron Scattering, *Phys. Rev. Lett.* **126**, 172502 (2021), arXiv:2102.10767 [nucl-ex].
- [3] D. Adhikari et al. (CREX), Precision Determination of the Neutral Weak Form Factor of ^{48}Ca , *Phys. Rev. Lett.* **129**, 042501 (2022), arXiv:2205.11593 [nucl-ex].
- [4] B. A. Brown, Constraints on the Skyrme Equations of State from Properties of Doubly Magic Nuclei, *Phys. Rev. Lett.* **111**, 232502 (2013), arXiv:1308.3664 [nucl-th].
- [5] I. Angeli and K. P. Marinova, Table of experimental nuclear ground state charge radii: An update, *Atom. Data Nucl. Data Tabl.* **99**, 69 (2013).
- [6] S. Tagami, T. Wakasa, J. Matsui, M. Yahiro, and M. Takechi, Neutron skin thickness of Pb208 determined from the reaction cross section for proton scattering, *Phys. Rev. C* **104**, 024606 (2021), arXiv:2010.02450 [nucl-th].
- [7] M. Toyokawa, M. Yahiro, T. Matsumoto, and M. Kohnno, Effects of chiral three-nucleon forces on ^4He -nucleus scattering in a wide range of incident energies, *PTEP* **2018**, 023D03 (2018), arXiv:1712.07033 [nucl-th].
- [8] S. Tagami, M. Tanaka, M. Takechi, M. Fukuda, and M. Yahiro, Chiral g -matrix folding-model approach to reaction cross sections for scattering of Ca isotopes on a C target, *Phys. Rev. C* **101**, 014620 (2020).
- [9] S. Tagami, T. Wakasa, and M. Yahiro, Neutron skin thickness of $^{116,118,120,122,124}\text{Sn}$ determined from reaction cross sections of proton scattering, *Results in Physics* **46**, 106296 (2023).
- [10] F. S. Dietrich et al., Proton Reaction Cross Sections Measured in the BNL/AGS E943 Experiment, *J. Nucl. Sci. Tech.* **39**, 269 (2002).
- [11] P. Renberg, D. Measday, M. Pepin, P. Schwaller, B. Favier, and C. Richard-Serre, Reaction cross sections for protons, *Nuclear Physics A* **183**, 81 (1972).
- [12] J. M. Cassels and J. D. Lawson, Absorption cross sections for 134 mev protons, *Proceedings of the Physical Society. Section A* **67**, 125 (1954).
- [13] P. Kirkby and W. T. Link, *Canadian Journal of Physics* **44**, 1847 (1966), <https://doi.org/10.1139/p66-155>.
- [14] R. Goloskie and K. Strauch, Measurement of proton inelastic cross sections, *Nuclear Physics* **29**, 474 (1962).
- [15] V. Meyer, R. M. Eisberg, and R. F. Carlson, Total reaction cross sections of several nuclei for protons, *Phys. Rev.* **117**, 1334 (1960).
- [16] T. Gooding, Proton total reaction cross sections at 34 mev, *Nuclear Physics* **12**, 241 (1959).
- [17] R. Abegg, J. Birchall, N. Davison, M. de Jong, D. Ginther, D. Hasell, T. Nasr, W. van Oers, R. Carlson, and A. Cox, Measurement of the proton total reaction cross section for ^{159}Tb , ^{181}Ta and ^{197}Au between 20 and 48 Mev, *Nuclear Physics A* **324**, 109 (1979).
- [18] T. Suzuki et al., Neutron skin of Na isotopes studied via the interaction cross-sections, *Phys. Rev. Lett.* **75**, 3241 (1995).
- [19] T. Suzuki et al., Nuclear radii of Na and Mg isotopes, *Nucl. Phys. A* **630**, 661 (1998).
- [20] G. Huber et al., Spins, magnetic moments, and isotope shifts of Na-21-31 by high resolution laser spectroscopy of the atomic D-1 line, *Phys. Rev. C* **18**, 2342 (1978), [Erratum: *Phys.Rev.C* **20**, 2457–2457 (1979)].
- [21] H. Zhang, W. Shen, Z. Ren, Y. Ma, W. Jiang, Z. Zhu, X. Cai, D. Fang, C. Zhong, L. Yu, Y. Wei, W. Zhan, Z. Guo, G. Xiao, J. Wang, J. Wang, Q. Wang, J. Li, M. Wang, and Z. Chen, Measurement of reaction cross section for proton-rich nuclei (a_j30) at intermediate energies, *Nuclear Physics A* **707**, 303 (2002).
- [22] A. Ozawa, T. Suzuki, and I. Tanihata, Nuclear size and related topics, *Nucl. Phys. A* **693**, 32 (2001).
- [23] A. Ozawa et al., Measurements of the interaction cross sections for Ar and Cl isotopes, *Nucl. Phys. A* **709**, 60 (2002), [Erratum: *Nucl.Phys.A* **727**, 465–466 (2003)].
- [24] M. Takechi, S. Suzuki, D. Nishimura, M. Fukuda, T. Ohtsubo, M. Nagashima, T. Suzuki, T. Yamaguchi, A. Ozawa, T. Moriguchi, H. Ohishi, T. Sumikama, H. Geissel, N. Aoi, R.-J. Chen, D.-Q. Fang, N. Fukuda, S. Fukuoka, H. Furuki, N. Inabe, Y. Ishibashi, T. Itoh, T. Izumikawa, D. Kameda, T. Kubo, M. Lantz, C. S. Lee, Y.-G. Ma, K. Matsuta, M. Mihara, S. Momota, D. Nagae, R. Nishikiori, T. Niwa, T. Ohnishi, K. Okumura, M. Ohtake, T. Ogura, H. Sakurai, K. Sato, Y. Shimbara, H. Suzuki, H. Takeda, S. Takeuchi, K. Tanaka, M. Tanaka, H. Uenishi, M. Winkler, Y. Yanagisawa, S. Watanabe, K. Minomo, S. Tagami, M. Shimada, M. Kimura, T. Matsumoto, Y. R. Shimizu, and M. Yahiro, Evidence of halo structure in ^{37}Mg observed via reaction cross sections and intruder orbitals beyond the island of inversion, *Phys. Rev. C* **90**, 061305 (2014).
- [25] S. Watanabe et al., Ground-state properties of neutron-rich Mg isotopes, *Phys. Rev. C* **89**, 044610 (2014), arXiv:1404.2373 [nucl-th].
- [26] S. Tagami, T. Wakasa, and M. Yahiro, $^{12}\text{C}+^{12}\text{C}$ scattering as the reference system for reaction cross section, *Results in Physics* **51**, 106675 (2023).
- [27] T. Wakasa, M. Takechi, S. Tagami, and M. Yahiro, Matter radii and skins of $^6,8\text{He}$ from reaction cross section of proton+ $^6,8\text{He}$ scattering based on the love-franey t-matrix model, *Results in Physics* **35**, 105329 (2022).
- [28] M. Takechi, M. Fukuda, M. Mihara, K. Tanaka, T. Chinda, T. Matsumasa, M. Nishimoto, R. Matsumiya, Y. Nakashima, H. Matsubara, K. Matsuta, T. Minamisono, T. Ohtsubo, T. Izumikawa, S. Momota, T. Suzuki, T. Yamaguchi, R. Koyama, W. Shinozaki, M. Takahashi, A. Takizawa, T. Matsuyama, S. Nakajima, K. Kobayashi, M. Hosoi, T. Suda, M. Sasaki, S. Sato, M. Kanazawa, and A. Kitagawa, Reaction cross sections at intermediate energies and fermi-motion effect, *Phys. Rev. C* **79**, 061601 (2009).
- [29] T. Wakasa, S. Tagami, J. Matsui, M. Takechi, and M. Yahiro, Neutron-skin values and matter and neutron radii determined from reaction cross sections of proton scattering, *Phys. Rev. C* **107**, 024608 (2023), arXiv:2211.16688 [nucl-th].
- [30] W. G. Love and M. A. Franey, *Phys. Rev. C* **24**, 1073 (1981).
- [31] M. Takechi, T. Ohtsubo, M. Fukuda, D. Nishimura, T. Kuboki, T. Suzuki, T. Yamaguchi, A. Ozawa, T. Moriguchi, H. Oishi, D. Nagae, H. Suzuki, S. Suzuki, T. Izumikawa, T. Sumikama, M. Ishihara, H. Geissel, N. Aoi, R.-J. Chen, D.-Q. Fang, N. Fukuda, I. Hachiuma, N. Inabe, Y. Ishibashi, Y. Ito, D. Kameda, T. Kubo, K. Kusaka, M. Lantz, Y.-G. Ma, K. Matsuta, M. Mihara, Y. Miyashita, S. Momota, K. Namihira, M. Nagashima, Y. Ohkuma, T. Ohnishi, M. Ohtake, K. Ogawa, H. Sakurai, Y. Shimbara, T. Suda, H. Takeda, S. Takeuchi, K. Tanaka, R. Watanabe, M. Winkler, Y. Yanagisawa, Y. Yasuda, K. Yoshinaga, A. Yoshida, and K. Yoshida, Interaction cross sections for ne isotopes towards the island of inversion

- and halo structures of ^{29}Ne and ^{31}Ne , *Physics Letters B* **707**, 357 (2012).
- [32] K. Minomo, T. Sumi, M. Kimura, K. Ogata, Y. R. Shimizu, and M. Yahiro, Determination of the structure of ^{31}Ne by a fully microscopic framework, *Phys. Rev. Lett.* **108**, 052503 (2012).
- [33] T. Sumi, K. Minomo, S. Tagami, M. Kimura, T. Matsumoto, K. Ogata, Y. R. Shimizu, and M. Yahiro, Deformation of ne isotopes in the region of the island of inversion, *Phys. Rev. C* **85**, 064613 (2012).
- [34] M. Tanaka *et al.*, Swelling of Doubly Magic ^{48}Ca Core in Ca Isotopes beyond $N = 28$, *Phys. Rev. Lett.* **124**, 102501 (2020), arXiv:1911.05262 [nucl-ex].
- [35] M. Takechi, T. Wakasa, S. Tagami, J. Matsui, and M. Yahiro, Reanalyzes for $^{42-51}\text{Ca}$ scattering on a ^{12}C target at 280 mev/nucleon based on chiral g folding mode with gognyd1s hartree–fock–bogoliubov densities, *Results in Physics* **31**, 104923 (2021).
- [36] E. Chabanat, P. Bonche, P. Haensel, J. Meyer, and R. Schaefer, A Skyrme parametrization from subnuclear to neutron star densities. 2. Nuclei far from stabilities, *Nucl. Phys. A* **635**, 231 (1998), [Erratum: *Nucl.Phys.A* 643, 441–441 (1998)].
- [37] N. Schunck *et al.*, Solution of the Skyrme–Hartree–Fock–Bogolyubov equations in the Cartesian deformed harmonic-oscillator basis. (VIII) hfodd (v2.73y): A new version of the program, *Comput. Phys. Commun.* **216**, 145 (2017), arXiv:1612.05314 [nucl-th].
- [38] M. Matsuzaki, S. Tagami, and M. Yahiro, Neutron skin thickness of ^{208}Pb , $^{116,120,124}\text{Sn}$, and ^{40}Ca determined from reaction cross sections of ^4He scattering, *Phys. Rev. C* **104**, 054613 (2021), arXiv:2107.06441 [nucl-th].
- [39] R. Carlson, A. Cox, T. Nasr, M. De Jong, D. Ginther, D. Hasell, A. Sourkes, W. van Oers, and D. Margaziotis, Measurements of proton total reaction cross sections, *Nuclear Physics A* **445**, 57 (1985).
- [40] F. A. . Brieva and J. Rook, *Nucl. Phys.* **A291**, 299 (1977).
- [41] K. Amos, P. J. Dortmans, H. V. von Geramb, S. Karataglidis, and J. Raynal, *Advances in Nuclear Physics*, edited by J. W. Negele and E. Vogt, Vol. 25 (Plenum, New York, 2000) p. 275.
- [42] T. Furumoto, Y. Sakuragi, and Y. Yamamoto, *Phys. Rev. C* **78**, 044610 (2008).
- [43] T. Sumi, K. Minomo, S. Tagami, M. Kimura, T. Matsumoto, K. Ogata, Y. R. Shimizu, and M. Yahiro, Deformation of Ne isotopes in the island-of-inversion region, *Phys. Rev. C* **85**, 064613 (2012), arXiv:1201.2497 [nucl-th].
- [44] M. Toyokawa, K. Minomo, and M. Yahiro, Mass-number and isotope dependence of local microscopic optical potentials for polarized proton scattering, *Phys. Rev. C* **88**, 054602 (2013).
- [45] K. Egashira, K. Minomo, M. Toyokawa, T. Matsumoto, and M. Yahiro, Microscopic optical potentials for ^4He scattering, *Phys. Rev. C* **89**, 064611 (2014), arXiv:1404.2735 [nucl-th].
- [46] M. Toyokawa, K. Minomo, M. Kohno, and M. Yahiro, Roles of chiral three-nucleon forces in nucleon–nucleus scattering, *J. Phys. G* **42**, 025104 (2015), [Erratum: *J.Phys.G* 44, 079502 (2017)], arXiv:1404.6895 [nucl-th].
- [47] M. Toyokawa, M. Yahiro, T. Matsumoto, K. Minomo, K. Ogata, and M. Kohno, Microscopic calculations based on chiral two- and three-nucleon forces for proton- and ^4He -nucleus scattering, *Phys. Rev. C* **92**, 024618 (2015), [Erratum: *Phys.Rev.C* 96, 059905 (2017)], arXiv:1507.02807 [nucl-th].
- [48] G. R. Satchler and W. G. Love, Folding model potentials from realistic interactions for heavy-ion scattering, *Phys. Rept.* **55**, 183 (1979).
- [49] M. Kohno, *Phys. Rev. C* **88**, 064005 (2013).
- [50] J. Fujita and H. Miyazawa, Pion Theory of Three-Body Forces, *Prog. Theor. Phys.* **17**, 360 (1957).
- [51] H. V. von Geramb *et al.*, *Phys. Rev. C* **44**, 73 (1991).
- [52] K. Amos and P. J. Dortmans, *Phys. Rev. C* **49**, 1309 (1994).
- [53] K. Minomo, K. Ogata, M. Kohno, Y. R. Shimizu, and M. Yahiro, The Brieva-Rook Localization of the Microscopic Nucleon-Nucleus Potential, *J. Phys. G* **37**, 085011 (2010), arXiv:0911.1184 [nucl-th].
- [54] N. Yamaguchi, S. Nagata, and T. Matsuda, *Prog. Theor. Phys.* **70**, 459 (1983).
- [55] H. de Vries, C. W. de Jager, and C. de Vries, NUCLEAR CHARGE-DENSITY-DISTRIBUTION PARAMETERS, *At. Data Nucl. Data Tables* **36**, 495 (1987).
- [56] S. Tagami, T. Myo, and M. Yahiro, Neutron skin thickness of ^{208}Pb from total cross sections of neutron scattering at 14.137 mev and neutron skin thickness of ^{48}Ca , o, n, and c isotopes from reaction and interaction cross sections, *Phys. Rev. C* **110**, 064610 (2024).
- [57] S. Tagami, M. Tanaka, M. Takechi, M. Fukuda, and M. Yahiro, Chiral g -matrix folding-model approach to reaction cross sections for scattering of Ca isotopes on a C target, *Phys. Rev. C* **101**, 014620 (2020).